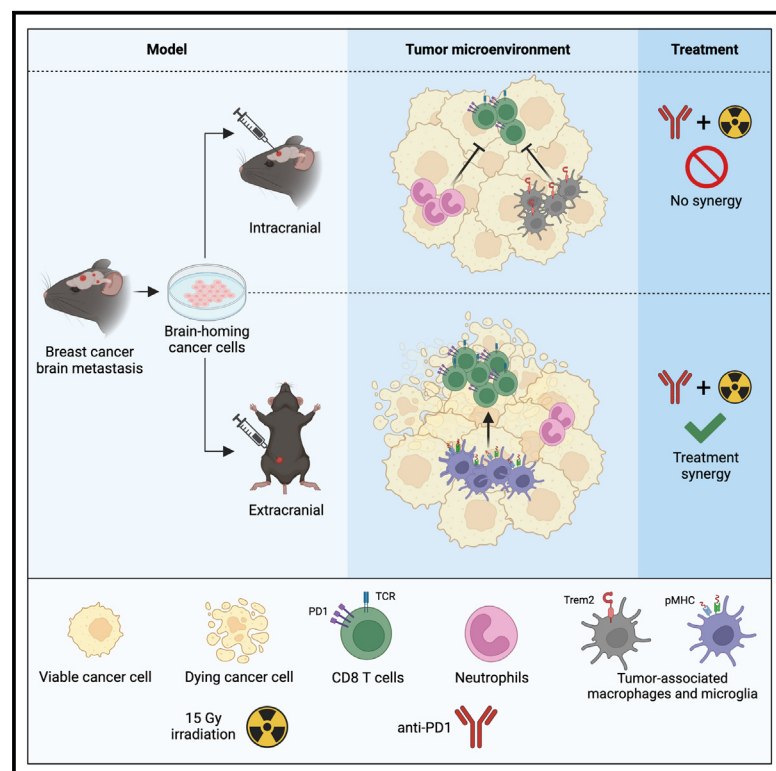# The local microenvironment suppresses the synergy between irradiation and anti-PD1 therapy in breast-to-brain metastasis

Graphical abstract

Authors

Vladimir Wischnewski,
Paola Guerrero Aruffo, Matteo Massara,
Roeltje R. Maas, Klara Soukup,
Johanna A. Joyce

Correspondence

vladimir.wischnewski@tron-mainz.de (V.W.),
johanna.joyce@unil.ch (J.A.J.)

In brief

Wischnewski et al. demonstrate suppressed CD8$^+$ T cell cytotoxicity in breast cancer brain metastases, contrasting with genetically identical extracranial tumors. Neutrophils and Trem2+ macrophages drive this suppression, limiting the efficacy of combined irradiation and anti-PD1 therapy, highlighting potential therapeutic targets for brain metastases.

Highlights

- CD8$^+$ T cells infiltrate breast cancer brain metastases

- Depletion of CD8$^+$ T cells accelerates extracranial, but not intracranial, tumor growth

- Anti-PD1 plus irradiation synergizes in extracranial, but not intracranial, tumors

- Neutrophils and Trem2+ macrophages in the brain TME suppress T cell function

CellPress

Report

The local microenvironment suppresses the synergy between irradiation and anti-PD1 therapy in breast-to-brain metastasis

Vladimir Wischnewski,[1,2,3,4,*] Paola Guerrero Aruffo,[1,2,3,4] Matteo Massara,[1,2,3,4] Roeltje R. Maas,[1,2,3,4,5,6] Klara Soukup,[1,2,3] and Johanna A. Joyce[1,2,3,4,7,*]

[1]Department of Oncology, University of Lausanne, CH 1011 Lausanne, Switzerland
[2]Ludwig Institute for Cancer Research, University of Lausanne, CH 1011 Lausanne, Switzerland
[3]Agora Cancer Research Centre Lausanne, CH 1011 Lausanne, Switzerland
[4]Lundin Family Brain Tumor Research Center, Departments of Oncology and Clinical Neurosciences, Centre Hospitalier Universitaire Vaudois, CH 1011 Lausanne, Switzerland
[5]Neuroscience Research Center, Centre Hospitalier Universitaire Vaudois, CH 1011 Lausanne, Switzerland
[6]Department of Neurosurgery, Centre Hospitalier Universitaire Vaudois, CH 1011 Lausanne, Switzerland
[7]Lead contact
*Correspondence: vladimir.wischnewski@tron-mainz.de (V.W.), johanna.joyce@unil.ch (J.A.J.)
https://doi.org/10.1016/j.celrep.2025.115427

SUMMARY

The brain environment is uniquely specialized to protect its neuronal tissue from excessive inflammation by tightly regulating adaptive immunity. However, in the context of brain cancer progression, this regulation can lead to a conflict between T cell activation and suppression. Here, we show that, while CD8+ T cells can infiltrate breast cancer-brain metastases, their anti-tumor cytotoxicity is locally suppressed in the brain. Conversely, CD8+ T cells exhibited tumoricidal activity in extracranial mammary lesions originating from the same cancer cells. Consequently, combined high-dose irradiation and anti-programmed cell death protein 1 (PD1) therapy was effective in extracranial tumors but not intracranial lesions. Transcriptional analyses and functional studies identified neutrophils and Trem2-expressing macrophages as key sources for local T cell suppression within the brain, providing rational targets for future therapeutic strategies.

INTRODUCTION

Metastatic dissemination to the brain occurs in approximately one-third of patients with breast cancer (BC) and can lead to life-threatening neurological damage.[1] Stereotactic radiosurgery (SRS), a standard-of-care treatment for brain metastasis (BrM), controls over 80% of targeted lesions.[2] However, the emergence of new BrM lesions outside the irradiation field and progression of extracranial disease limit median overall survival to just over 1 year.[3] Combining SRS with systemic treatment modalities offers a promising strategy to improve the prognosis of patients with BC-BrM, as similar approaches have shown efficacy in managing extracranial BC metastasis.[4] Currently, chemotherapy, targeted therapy, and immunotherapy are being studied as combination partners for SRS and other forms of radiotherapy (RT) in the clinic.[5,6] However, much of our understanding about the mode of action of these systemic treatment modalities comes from studies of extracranial tumors or primary brain cancers. By contrast, the response of BrM to such interventions is not well understood.

In addition to the intrinsic sensitivity of tumor cells to therapy, the local tumor microenvironment (TME) plays a critical role in regulating treatment response.[7] This complex and dynamic ecosystem of cellular and non-cellular components varies substantially between tumor types and anatomical locations. For

instance, we observed that the efficacy of BLZ945, an inhibitor of colony stimulating factor 1 receptor (CSF1R) signaling in macrophages, varies considerably between tumor types even within the same anatomical location. BLZ945 was very effective in regressing primary brain tumors[8] but showed minimal efficacy as a monotherapy against BrM.[9] Similarly, in a study using a melanoma metastasis model, the therapeutic efficacy of anti-programmed cell death protein 1 (PD1) plus anti-cytotoxic T-lymphocyte associated protein 4 (CTLA4) combination therapy depended on the anatomical location of the lesions, despite originating from identical cancer cells.[10]

The BrM TME is composed of brain-intrinsic cells and structures, including the blood-brain barrier, astrocytes, and microglia, as well as immune cells infiltrating from the periphery or the meninges, such as monocyte-derived macrophages (MDMs), neutrophils,[11,12] and T cells.[13,14] Brain astrocytes and myeloid cells, in particular, influence the efficacy of RT and immunotherapy in preclinical models and early clinical trials.[9,15–18] Overall, the brain TME is recognized as an immunologically "cold" or immune-suppressed microenvironment.[7,19]

In this study, we show that, while CD8+ T cells infiltrate BC-BrM, they lack anti-tumor cytotoxicity even under T cell-stimulating conditions. Single-cell profiling and ex vivo functional assays identified BrM-infiltrating neutrophils and triggering receptor
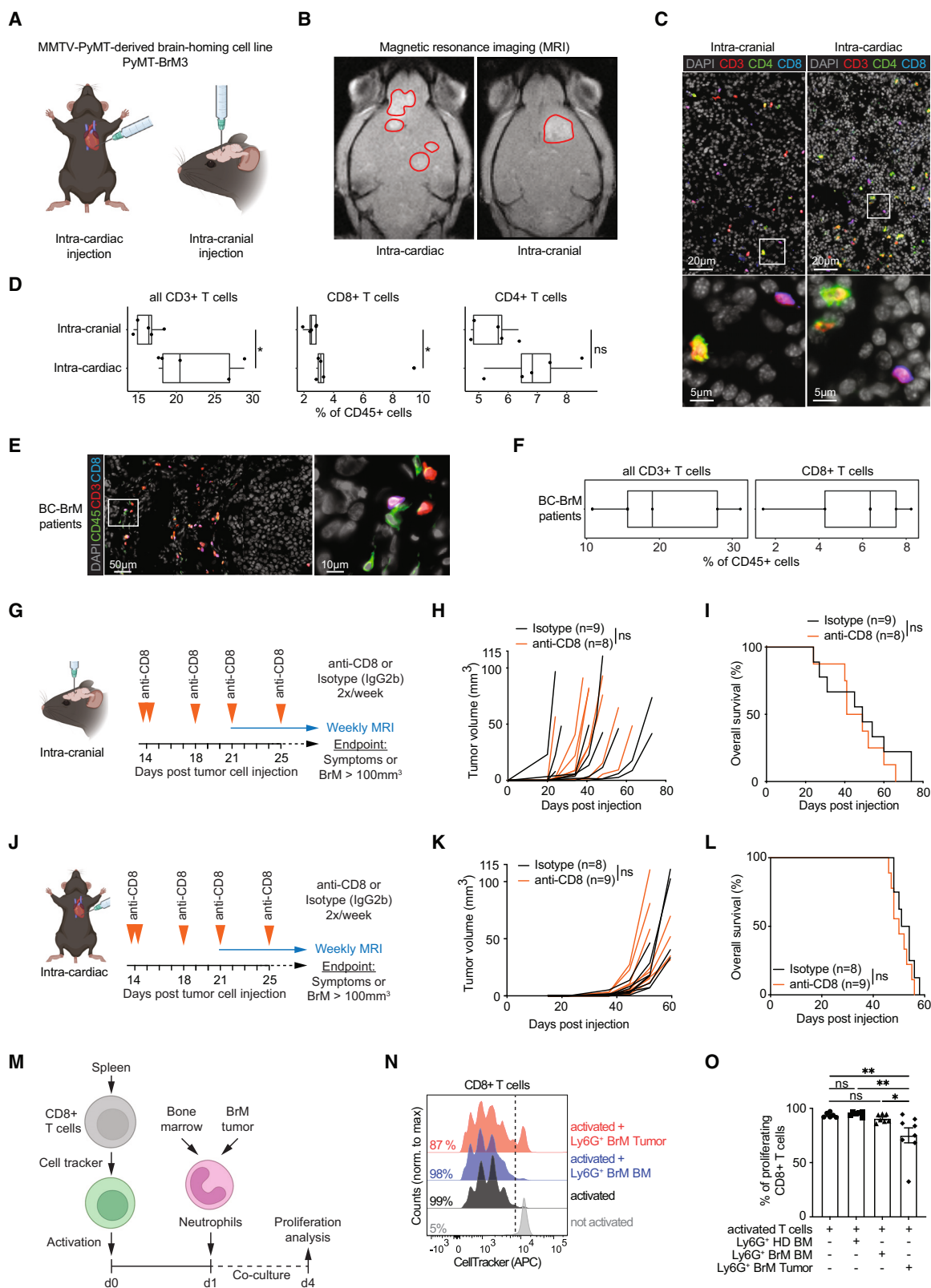
(legend on next page)

expressed on myeloid cells 2 (Trem2)+ MDMs and microglia (collectively termed tumor-associated macrophages [TAMs]) as key sources of local T cell suppression.

RESULTS

BC-BrM tumor growth is independent of CD8+ T cells in both intracardiac and intracranial models

To study the effects of combining localized BrM irradiation with T cell-targeted therapies, a tumor model with a well-defined lesion location, lesion number, and evident T cell infiltration is necessary. We thus adapted our recently described mouse model of BC-BrM by injecting the brain-homing PyMT-BrM3 cell line[20] intracranially to generate a defined lesion (Figure 1A). This approach resulted in a single BrM in the right frontal cortex (Figure 1B, right panel), contrasting with the multifocal lesions that develop following intracardiac injection of metastatic tumor cells (Figure 1B, left panel).

We compared the abundance of T cells in these two models by immunofluorescence (IF) staining and imaging of tumor tissue sections. We found comparable, yet moderately lower, proportions (Figures 1C and 1D) and numbers (Figure S1A) of total CD3+, CD4+, and CD8+ T cells in BrM derived from intracranial injection. Importantly, the proportions and numbers of CD3+ and CD8+ T cells in both models were similar to those observed in our analysis of patient BC-BrM samples (Figures 1E, 1F, and S1B). Flow cytometry (FCM) analysis of CD45+ leukocytes in volume-matched tumors confirmed the comparable proportions of T cells in both models (Figures S1C–S1G). A substantially higher proportion of microglia (MG) was observed in tumors resulting from intracardiac injection (Figures S1D and S1E). We attribute this difference, at least in part, to the technical challenge of cleanly dissecting out small BrM lesions after intracardiac inoculation. The surrounding tissue, which is highly infiltrated with ionized calcium-binding adapter molecule 1 (Iba1)+ myeloid cells (including MG), cannot be removed completely and this results in somewhat elevated MG proportions in tumors derived from intracardiac injections (Figure S1H).

To determine whether CD8+ T cells were involved in tumor control, we depleted these cells from BrM-bearing mice using an antibody-based approach. Treatment was started 14 days after BrM cell injection, a time point before expansive tumor

growth was detectable by magnetic resonance imaging (MRI) (Figure 1G). Clear efficacy of CD8+ T cell depletion was observed in the blood, lymphoid organs, and brain tumors 1 week post treatment (day 21 post tumor cell injection) and also toward the end of the trial at day 50 (Figures S1I–S1K). However, CD8+ T cell depletion did not significantly impact BrM growth or mouse survival in either the intracranial (Figures 1H and 1I) or intracardiac models (Figures 1J, 1K, and 1L).

The absence of evident CD8+ T cell-mediated anti-tumor immunity in these BC-BrM models is suggestive of immune-suppression within the brain TME. Myeloid cells are major contributors to immunosuppression in different cancers,[21–23] and neutrophils are among the most abundant myeloid populations in the BrM TME in both humans and mice (Figures S1D and S1E).[12,24] Neutrophils have also been shown to function as potent immune-suppressive cells.[25] We therefore evaluated the ability of neutrophils to inhibit T cell proliferation using an *ex vivo* suppression assay (Figure 1M). Bone marrow (BM)-derived neutrophils isolated from either healthy (HD) or BrM-bearing mice did not alter the proliferation of T cells, which had been activated by pre-treatment with anti-CD3/anti-CD28 antibodies (Figures 1N and 1O). By contrast, tumor-associated neutrophils (TANs) freshly isolated from BrM lesions significantly reduced the proportion of proliferating T cells, indicating potential suppressive activity within the BrM TME *in vivo* (Figures 1N and 1O). In sum, while CD8+ T cells are present in BC-BrM lesions, their quantity and/or quality are insufficient to elicit anti-tumor immunity, with TANs representing one potential source of T cell suppression.

The transient elevation in the lymphoid:myeloid ratio following irradiation does not lead to synergy with anti-PD1 treatment

To evaluate whether localized, high-dose, hypo-fractionated RT enhances anti-tumor T cell immunity in BC-BrM, we first established a treatment protocol to mimic clinically relevant BrM-RT, which is most commonly delivered in a single fraction of 12–24 Gy.[26] We tested a 10- to 40-Gy dose range on BrM cells *in vitro* and observed a dose-dependent tumoricidal activity plateauing at doses ≥20 Gy (Figure S2A). Next, we developed a treatment protocol to precisely irradiate BrM lesions in mice in a focalized manner, avoiding damage to the eyes, cerebellum, and

Figure 1. Growth of BC-BrM is independent of CD8+ T cells in both intracardiac and intracranial models

(A) Schematic of tumor models.

(B) Representative magnetic resonance (MR) images of BC-BrM arising from intracardiac or intracranial injection of the PyMT-BrM3 cell line (left and right, respectively).

(C and D) Representative immunofluorescence (IF) images (C) and quantification (D) of T cell populations in intracardiac or intracranial BrM lesions as a proportion of total CD45+ immune cells (*n* = 5 mice per group). Statistical significance determined using the Mann-Whitney U test. Scale bars are indicated in the figure; either 20 μm (top) or 5 μm (bottom).

(E and F) Representative IF images (E) and quantification (F) of T cells in BrM tumors from BC patients (*n* = 5). Scale bars are indicated in the figure; either 50 μm (left) or 10 μm (right).

(G–I) Schematic (G), tumor growth curves of individual mice (H) and Kaplan-Meier survival plots (I) of antibody-mediated CD8+ T cell depletion in BrM-bearing mice (intracranial model). Significance determined using the type II ANOVA test (H) and the log rank test (I) with *n* = 9 isotype-treated and *n* = 8 anti-CD8-treated mice.

(J–L) Schematic (J), tumor growth curves of individual mice (K), and Kaplan-Meier survival plots (L) of antibody-mediated CD8+ T cell depletion in BrM-bearing mice (intracardiac model). Statistical significance determined using the type II ANOVA test (K) and the log rank test (L) with *n* = 8 isotype-treated and *n* = 9 anti-CD8-treated mice.

(M–O) Schematic (M), representative histograms (N), and quantification (O) of T cell proliferation in co-cultures with Ly6G+ neutrophils from the indicated BM or BrM tumor sources. Statistical significance determined using Kruskal-Wallis test and *post hoc* analysis with Benjamini-Hochberg correction. ns, non-significant; *p* or adjusted *p* (*p*.adj) >0.05; *p or *p*.adj <0.05; **p or *p*.adj <0.01.
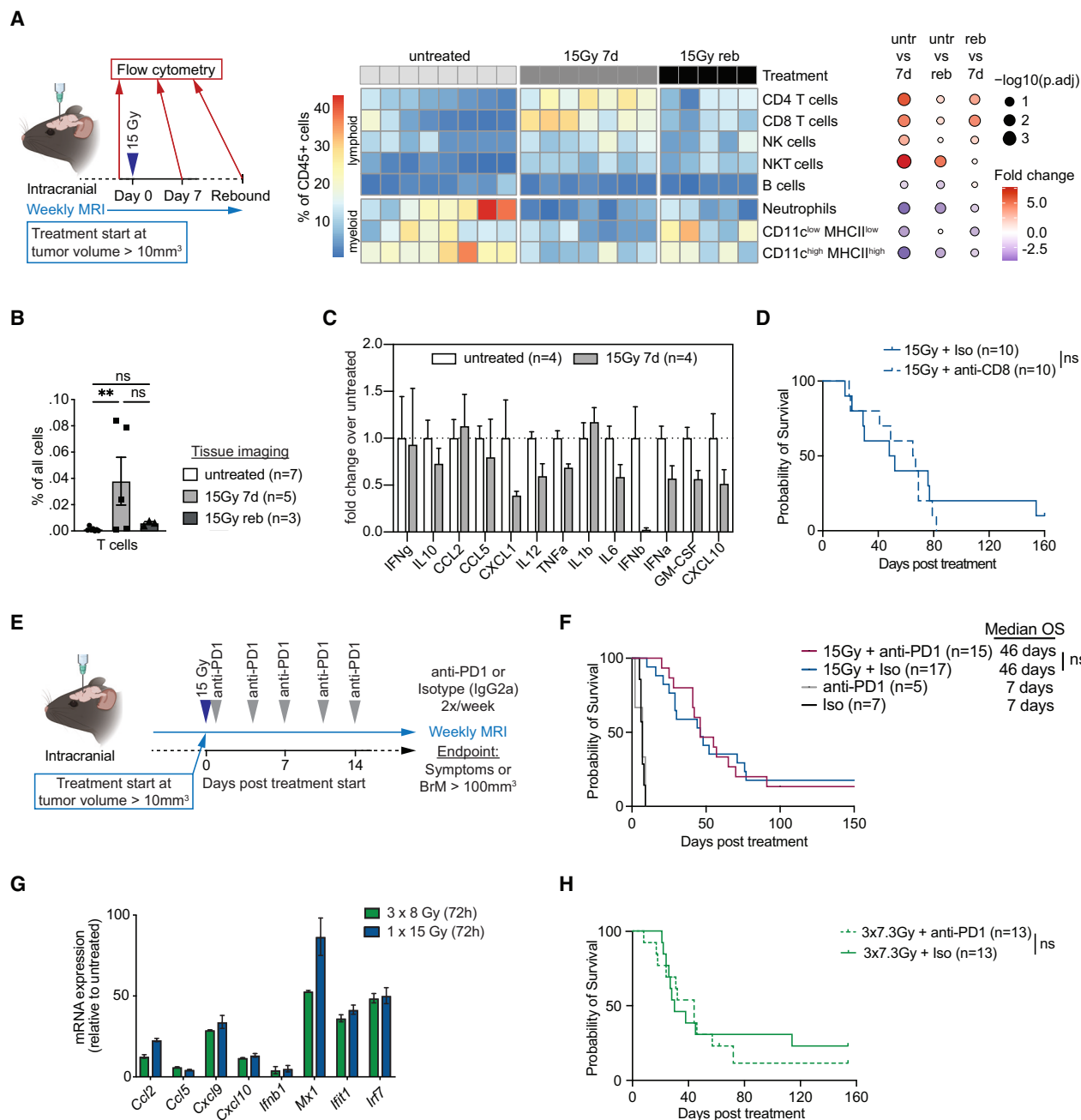
Figure 2. Brain irradiation induces changes in the BrM-TME but does not synergize with anti-PD1 treatment

(A) Schematic and heatmap showing the quantification of immune cells in BrM tumors analyzed by flow cytometry (FCM). n = 5–8 mice per time point; each column represents an individual mouse sample. Fold changes and adjusted p values are displayed as dot plots on the right. Statistical significance determined using Kruskal-Wallis test and *post hoc* analysis with Benjamini-Hochberg correction.

(B) Quantification of CD3$^+$ T cells by IF staining and image analysis at the indicated time points following 15-Gy RT. n = 5 mice per time point. Statistical significance determined using Kruskal-Wallis test and *post hoc* analysis with Benjamini-Hochberg correction.

(C) Bar plots visualizing cytokine bead array results showing changes in protein levels of the indicated molecules within BrM tumors 7 days following 15-Gy RT (n = 4 mice per treatment group). Data shown as mean ± standard error of the mean of the fold change compared to untreated mice.

(D) Antibody-mediated CD8$^+$ T cell depletion was performed in BrM-bearing mice, starting 1 day before the delivery of 15-Gy RT. Data are shown as Kaplan-Meier survival plots with n = 10 mice in each treatment group. Statistical significance was determined using the log rank test.

(E and F) Schematic (E) and Kaplan-Meier survival plots (F) of combined treatment of BrM-bearing mice with 15-Gy RT and anti-PD1 antibody. Data from two independent experiments were pooled and are shown as Kaplan-Meier survival plots. The number of mice in each treatment group is indicated on the graph. Statistical significance determined using the log rank test.

(legend continued on next page)

masticatory apparatus, by combining MRI and computed tomography (CT)-guided RT administration (Figure S2B). This treatment was performed during the exponential growth phase of BrM (tumor volumes >10 mm³), and we compared the efficacy of 10-, 15-, and 20-Gy doses. Consistent with the *in vitro* experiments, we found a dose-dependent improvement in tumor control and survival *in vivo* (Figures S2C and S2D). However, higher doses also led to transient alopecia at the irradiation site (Figures S2E and S2F), leading us to select 15 Gy as the optimal dose.

We then assessed potential immune cell alterations in the BrM TME 7 days after 15 Gy RT by FCM. We observed a significant increase in the proportion of T and natural killer T (NKT) cells, as well as a decrease in the myeloid compartment, with neutrophils showing the most significant changes (Figure 2A). These changes were mostly transient, however, and returned to the initial baseline values at tumor relapse (Figure 2A). Using IF analysis, we confirmed the transient increase of T cells shortly after 15 Gy RT (Figures 2B and S2G). Despite the elevated lymphoid: myeloid ratio, we observed a reduction in levels of pro-inflammatory cytokines 7 days post RT (Figure 2C), indicating a more complex suppression of anti-tumor immunity in the BrM TME. Moreover, we found that the therapeutic efficacy of 15 Gy RT was independent of CD8⁺ T cells, as it was unaffected by anti-CD8 antibody treatment (Figures 2D and S3A).

We next investigated whether the PD1-programmed cell death ligand 1 (PDL-1) immune checkpoint pathway might be involved in mediating T cell suppression, and therefore combined RT with anti-PD1 treatment (Figure 2E). Critically, we confirmed that all PD1+ T cells in BrM tumors and draining lymph nodes (LNs) were coated with therapeutic anti-PD1 antibodies *in vivo* (Figure S3B). Nonetheless, anti-PD1 treatment alone had no therapeutic effect and did not further improve the efficacy of RT, despite an initial survival advantage in the treatment combination group (Figure 2F). Of note, the transient modest effect on survival following combination therapy inversely correlated with the tumor volume at treatment onset, with smaller tumors initially responding better (Figure S3C).

Although the anti-PD1 antibody (RMP1-14) used here is commonly employed in preclinical research, it is a rat IgG2a clone. In contrast, therapeutic anti-PD1 antibodies in the clinic are usually human or humanized. To exclude the possibility that the absence of evident anti-PD1 efficacy is due to the source of the antibody, we also evaluated a murinized, and more potent, version of RMP1-14 (mIgG1e3). However, similar results were observed with this murine molecule both as monotherapy (Figure S3E) and in combination with RT (Figure S3F), indicating the inherent resistance to anti-PD1 treatment in the BrM model.

Preclinical studies in extracranial tumors have reported that fractionating RT can enhance systemic synergy with immunotherapy, partly due to increased interferon signaling.[27,28] Therefore, we evaluated RT delivered in three fractions of 7.3 Gy (or 3 × 8 Gy for *in vitro* experiments), corresponding to a biologically effective dose equivalent to 1 × 15 Gy. The expression of interferon-stimulated genes in the BrM model was similarly induced by both 1 × 15 Gy and 3 × 8 Gy *in vitro* (Figure 2G). The therapeutic efficacy of 3 × 7.3 Gy was comparable to that of 1 × 15 Gy and was also not enhanced by the addition of anti-PD1 (Figure 2H). Additionally, reducing the RT dose to 2 × 5 Gy did not induce synergy with anti-PD1 (Figure S3D). Together, these findings suggest there is an anti-PD1 resistance mechanism in the BC-BrM model that cannot be overcome by RT despite this treatment inducing theoretically favorable immune cell alterations in the TME.

RT acts synergistically with anti-PD1 in BC-BrM cell-derived tumors growing outside of the brain and induces a pro-inflammatory environment

To determine whether anti-PD1 resistance was mediated by the cancer cells or the brain microenvironment, we established extracranial tumors using the same BC-BrM cell line and injecting the cells into the mammary fat pad (MFP, the orthotopic primary site of the BC-BrM model). Using CT imaging, we verified a safe distance between MFP tumors and the nearest draining lymph nodes, ensuring precise irradiation of only the cancerous tissue (Figure S4A). MFP tumors were treated at volumes >100 mm³ (Figure S4A). While this volume is 10 times larger than that of treated BrM (BrM > 10 mm³), it represents the exponential growth phase in the MFP setting, thus corresponding to a similar tumor stage as for when the irradiation was administered to BrM lesions.

First, we examined potential alterations in the MFP TME 7 days post RT and observed a trend toward a transient increase in the T cell:neutrophil ratio, similar to that seen in BrM (Figures 3A and 3B). However, unlike the intracranial tumors (Figure 1C), the levels of pro-inflammatory molecules such as interferon-beta were elevated up to 4-fold 7 days after RT in MFP tumors (Figure 3C), indicating the potent induction of an inflammatory environment. Next, we treated MFP tumor-bearing mice with the same combination of anti-PD1 plus RT (Figures 3D and S4B) as for BrM-bearing mice above. While anti-PD1 treatment alone had no effect on survival, RT significantly improved the outcome for MFP tumor-bearing mice (Figure 3E). Notably, in contrast to the combination treatment in the brain, MFP tumors responded significantly better to anti-PD1 plus RT compared to RT alone (Figure 3E), suggesting a synergistic effect between the two therapies. In sum, combined RT and anti-PD1 treatment act synergistically in BC-BrM-derived tumors growing outside of the brain, but not inside, indicating that anti-PD1 resistance is mediated by the specific TME in the brain.

Differences in the cellular composition of the intracranial versus extracranial TME inform potential mechanisms of anti-PD1 resistance in BrM

To identify potential mechanisms driving anti-PD1 resistance in the brain, we compared the CD45⁺ leukocyte populations in intracranial and extracranial tumors using FCM and single-cell

---

(G) RT-qPCR analysis of interferon-stimulated gene expression in the PyMT-BrM3 cell line after indicated RT treatment *in vitro*. Data shown as mean ± standard deviation of the fold change difference in expression compared to untreated cells. Two biological replicates. AU, arbitrary units.

(H) Kaplan-Meier survival plot of combined treatment of BrM-bearing mice with 3 × 7.3-Gy RT and anti-PD1. Data from two independent experiments were pooled. Number of mice in each treatment group is indicated. Significance determined with the log rank test. ns, *p*.adj >0.05; **p*.adj < 0.05; ***p*.adj < 0.01; ****p*.adj < 0.001. Overall survival, OS.
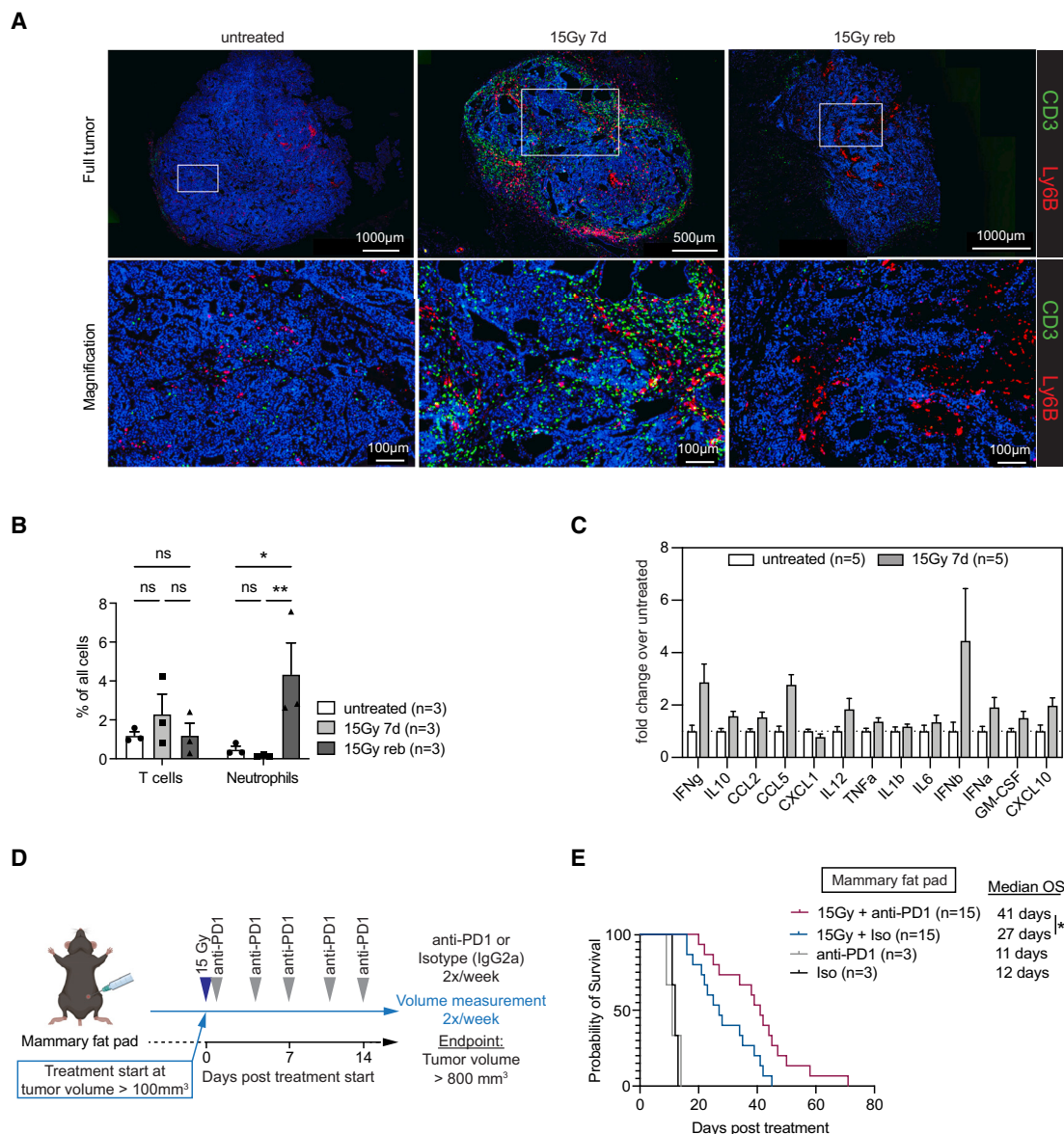
Figure 3. 15-Gy RT acts synergistically with anti-PD1 treatment in BC-BrM-derived tumors growing outside of the brain and induces a pro-inflammatory environment

(A) Representative IF images of CD3$^+$ T cells and Ly6B+ neutrophils at indicated time points following 15-Gy RT in the mammary fat pad (MFP) tumor model (BC-BrM cell line implanted in this location). Scale bars are indicated in the figure; either 500 μm and 1,000 μm (top) or 100 μm (bottom).

(B) Bar plots showing the quantification of CD3$^+$ T cells and Ly6B+ neutrophils in MFP tumors analyzed by IF (n = 3 mice). Statistical significance was determined using Kruskal-Wallis test and *post hoc* analysis with Benjamini-Hochberg correction. ns, p.adj > 0.05; *p.adj < 0.05; **p.adj < 0.01.

(C) Bar plots visualizing cytokine bead array results and showing changes in protein levels of the indicated molecules within MFP tumors 7 days following 15-Gy RT (n = 5 mice in each treatment group). Data shown as mean ± standard error of the mean of the fold change compared to untreated mice.

(D and E) Schematic (D) and Kaplan-Meier survival plot (E) of the 15-Gy plus anti-PD1 trial in MFP tumor-bearing mice. Data from two independent experiments were pooled. Number of mice in each treatment group is indicated. Statistical significance was determined using the log rank test. **p < 0.01.

RNA sequencing (scRNA-seq) (Figure 4A). FCM analysis revealed a significantly higher abundance of T and NKT cells in MFP tumors, along with the expected absence of brain-resident MG (Figure 4B). We hypothesized that elevated CD8$^+$ T cell levels in MFP tumors might indicate anti-tumor immunity and thus depleted these cells in the MFP model using the same strategy as in BrM tumors (Figures 4C and 1E). CD8$^+$ T cell depletion

in the MFP model significantly accelerated tumor growth, indicating that CD8$^+$ T cells indeed play a role in regulating extracranial tumor control (Figure 4D), in contrast to the absence of an effect when they were depleted in BrM.

Next, we analyzed the transcriptional profiles of tumor-infiltrating CD45$^+$ cells by scRNA-seq, detecting all major immune populations in both BrM and MFP tumors (Figures 4E and
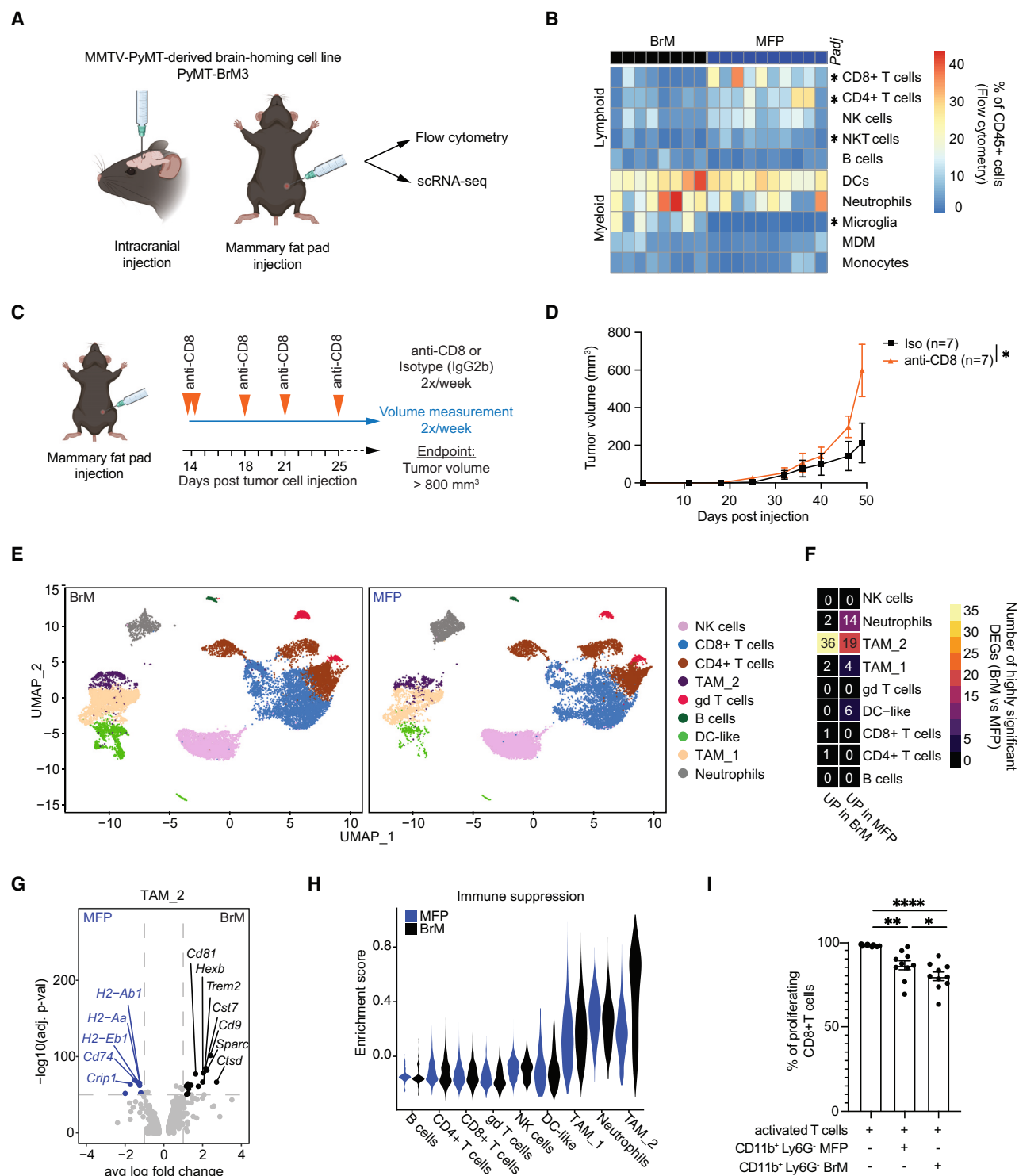
Figure 4. Extracranial mammary tumors show higher T cell infiltration compared to BrM and grow in a CD8⁺ T cell-dependent manner

(A) Schematic of tumor models and experimental design.

(B) Histogram summarizing the abundance of major immune cell populations in intracranial (BrM) and extracranial (MFP) tumors, as determined by FCM (n = 8–10 mice in each group). Statistical significance was determined using unpaired multiple t tests with Benjamini-Hochberg correction. *p.adj < 0.05.

(C and D) Schematic (C) and tumor growth curves (D) of antibody-mediated CD8⁺ T cell depletion in the MFP model (n = 7 mice per group). Statistical significance was determined using the type II ANOVA test.

(legend continued on next page)

S5A). Using a stringent cutoff of log2 fold change >1 | < −1 and adjusted *p* value <0.0001, minimal transcriptomic differences were observed in the lymphoid compartment, including CD8$^+$ and CD4$^+$ T cells, when comparing BrM and MFP tumors (Figures 4F and S5B; Table S1). Signatures of T cell activation, memory, and exhaustion were expressed to a similar extent. By contrast, highly significant transcriptional alterations were predominantly evident in myeloid cells, with one cluster of tumor-associated macrophages (TAM_2) showing the highest number of differentially expressed genes (Figures 4F, 4G, and S5C). Within the TAM_2 cluster, genes involved in antigen presentation, including members of the major histocompatibility complex (MHC) class II complex, were enriched in cells isolated from MFP tumors (Figure 4G). By contrast, BrM-infiltrating TAM_2 cells expressed higher levels of tetraspanins (*Cd9*, *Cd81*), proteolysis regulators (*Ctsd*, *Cst7*), and immune-suppression factors (*Trem2*) (Figure 4G). Of note, *Trem2* was expressed exclusively by TAMs, with the highest levels in the TAM_2 population (Figure S5D).

We hypothesized that BrM-infiltrating TAM_2 cells possess immune-suppressive activity. To test this, we devised and calculated an "immune-suppression" score based on the expression of known markers of TAM-mediated immune-inhibition (*Mrc1*, *Msr1*, *Cx3cr1*, *Marco*, *Siglec1*, *Trem2*, *Cd9*, *Cd63*, *Cd274*, *Nt5e*, *Mertk*). As expected, enrichment of the immune-suppression signature was observed in TAMs and neutrophils, with similar levels between BrM and MFP tumors in the TAM_1 and neutrophil populations, respectively (Figure 4H). By contrast, TAM_2 cells infiltrating BrM lesions displayed significantly higher levels of the immune-suppression signature when compared to MFP-infiltrating counterparts, as well as to all other immune populations in BrM (Figure 4H).

Finally, we evaluated the ability of CD11b+ Ly6G− cells composed of CD11c^{low} MHCII^{low} TAMs and CD11c^{high} MHCII^{high} dendritic cells (DCs) (Figure S4F) to suppress T cell proliferation *ex vivo* using the same experimental design as for neutrophils above. While both BrM- and MFP-infiltrating myeloid cells inhibited CD8$^+$ T cell proliferation, the suppressive effect was significantly higher in BrM-infiltrating cells, supporting our hypothesis (Figure 4I). Taken together, we have shown that the local TME in BC-BrM negatively influences T cell-mediated anti-tumor immunity, with neutrophils and TAMs representing important contributors to immune suppression.

DISCUSSION

In this study, we investigated the effects of localized, hypo-fractionated RT in the BrM-TME with a specific focus on enhancing the anti-tumor immune responses. We adapted a preclinical BC-BrM model and optimized RT protocols to mimic clinically relevant treatments. This adaptation was critical, as prior studies in this context often focused on hyper-fractionated whole-brain RT (WBRT, >5 fractions).[17,29] However, due to its comparable efficacy and improved side effect profile, hypo-fractionated RT in the form of SRS is now the preferred approach over WBRT for treating BrM.[30,31]

Our findings revealed that CD8$^+$ T cells infiltrate BrM lesions but fail to contribute to tumor control or enhance RT efficacy. We attribute this dysfunctional phenotype to the local brain TME, as we found that CD8$^+$ T cells in extracranial breast cancer lesions (established using the same cell line) effectively slowed tumor growth. Furthermore, while anti-PD1 treatment alone or combined with RT produced synergistic effects in extracranial tumors, this combination was ineffective in the brain TME.

Several mechanisms likely underlie the suboptimal T cell-mediated anti-tumor immune response in the brain, including impaired lymphatic drainage of brain-borne antigens,[10,32,33] inefficient T cell infiltration into the CNS,[34] and localized immune suppression.[35,36] Through a combination of FCM and scRNA-seq analyses, with *ex vivo* co-culture comparison of the TME between intracranial and extracranial tumors, we revealed S100a8/a9-expressing neutrophils and Trem2-expressing macrophages as key sources of T cell inhibition in the brain. In BrM patients, S100A8 and TREM2 expression identifies a distinct TAM population associated with immune suppression.[35] Myeloid cells with a similar phenotype have been associated with shorter survival and poor response to immune checkpoint blockade treatment in patients with extracranial cancers.[37,38] In mouse BrM models, targeting suppressive TAMs or disrupting their interaction with T cells improved survival, underscoring the pivotal role of TAMs in cranial immune suppression.[9,15]

Several strategies can be utilized to inhibit suppressive TAMs, including (1) preventing their recruitment, (2) depletion, and (3) phenotypic reprogramming.[21,22] Promising therapeutic targets include the CSF-1-CSF-1R axis,[8,9,39–41] the CCL2-CCR2 axis,[42–44] PI3Kγ,[45] and TREM1/2[46,47], with several of these therapies under translational investigation or clinically approved.[48] However, identifying a strategy that would specifically and effectively target the immune-suppressive TAM_2 population identified in this study requires future in-depth evaluation. Considerations such as brain-penetration capacity[49] and potentially a unique mode of action within the brain, as demonstrated for CSF-1R inhibition,[8,50,51] are critical.

Overall, this study highlights the challenges of translating therapies that have been shown to be effective in extracranial tumors to the brain, driven by its unique TME. These findings underscore

(E) Uniform manifold approximation and projection (UMAP) of single-cell RNA sequencing data from tumor-infiltrating immune cells in BrM and MFP tumors colored according to cell lineages (*n* = 3 mice in each group).

(F) Heatmap summarizing the number of differentially expressed genes (DEGs) in each cell population comparing gene expression in intracranial and extracranial tumor-infiltrating immune cells with log2 fold change >1 | < −1 and *p*.adj <0.0001.

(G) Log2(fold change) versus −log10(*p*.adj) volcano plot showing differential expression analysis contrasting TAM_2 cells from BrM to cells from MFP tumors, calculated with Seurat package in R. DEG with log fold change >1 | < −1 and −log10(*p*.adj) > 50 are highlighted.

(H) Violin plots summarizing the enrichment of a gene signature of immune suppression.

(I) Quantification of T cell proliferation in co-cultures with Ly6G− CD11b+ TAMs from the indicated sources. Statistical significance determined using ANOVA test and *post hoc* analysis with Benjamini-Hochberg correction. ns, *p*.adj > 0.05; *p.adj < 0.05; **p.adj < 0.01; ****p.adj < 0.0001.

the critical need for targeted strategies to overcome the specific immune-suppressive mechanisms within the brain TME.

Limitations of the study

There are some limitations to our study that should be considered. First, differences in tumor growth kinetics between intracranial and extracranial tumors may introduce bias. BrM growth is constrained by the skull, whereas MFP tumors grow relatively unrestricted, resulting in larger tumor volumes and distinct physicomechanical properties. To mitigate this, treatments were initiated when both MFP and BrM tumors reached exponential growth phases. However, it cannot be excluded that different tumor masses may still influence treatment responses. Second, our BrM mouse model lacks a concurrent primary tumor. Aggressive growth of even heavily pre-treated MFP tumors precluded the evaluation of long-term treatment responses in the brain within the same animals. Pre-exposure of the immune system to cancer antigens derived from a primary tumor may influence immunological response to different therapies. Future studies will be important to address these points and to further our understanding of BrM immune suppression and treatment resistance.

RESOURCE AVAILABILITY

Lead contact

Further information and requests for resources should be directed to the lead contact, Prof. Johanna A. Joyce (johanna.joyce@unil.ch).

Materials availability

The study did not generate new unique reagents.

Data and code availability

- The scRNA-seq data generated during this study have been deposited at Gene Expression Omnibus and are publicly available as of the date of publication. Mouse reference genome mm10 Ensembl 93 v3.1.0 (July 24, 2019) was used to align raw scRNA-seq reads and is publicly available. Accession numbers are listed in the key resources table.
- This paper does not report original code.
- Any additional information required to reanalyze the data reported in this paper is available from the lead contact upon request.

AUTHOR CONTRIBUTIONS

V.W. and J.A.J. conceived the study, designed experiments, interpreted data, and wrote the manuscript. V.W., P.G.A., M.M., R.R.M., and K.S. performed the experiments. V.W. performed all experimental analyses and prepared the figures. J.A.J. supervised the research. All authors reviewed and approved the manuscript.

STAR★METHODS

Detailed methods are provided in the online version of this paper and include the following:

- KEY RESOURCES TABLE
- EXPERIMENTAL MODEL AND STUDY PARTICIPANT DETAILS
  - Human brain metastasis samples
  - Mice
  - Cells
- METHOD DETAILS
  - Generation of experimental tumor models
  - Tumor growth monitoring
  - Radiation treatment of mice
  - Systemic treatment of mice
  - *In vitro* longitudinal cell viability measurement
  - Isolation of RNA from cultured cells, synthesis of cDNA and real-time PCR (qPCR)
  - Preparation of tissues from mice
  - Sectioning, staining and imaging of mouse tissues
  - Cytokine measurement
  - Flow cytometry
  - Sorting and encapsulating cells for single cell RNA-sequencing
  - Library preparation and data analysis for single-cell RNA sequencing
  - T cell-myeloid co-culture
- QUANTIFICATION AND STATISTICAL ANALYSIS

SUPPLEMENTAL INFORMATION

Supplemental information can be found online at https://doi.org/10.1016/j.celrep.2025.115427.

REFERENCES

1. Lin, N.U., Bellon, J.R., and Winer, E.P. (2004). CNS metastases in breast cancer. J. Clin. Oncol. *22*, 3608–3617. https://doi.org/10.1200/JCO.2004.01.175.

2. Mohammadi, A.M., Schroeder, J.L., Angelov, L., Chao, S.T., Murphy, E.S., Yu, J.S., Neyman, G., Jia, X., Suh, J.H., Barnett, G.H., and Vogelbaum, M.A. (2017). Impact of the radiosurgery prescription dose on the local control of small (2 cm or smaller) brain metastases. J. Neurosurg. *126*, 735–743. https://doi.org/10.3171/2016.3.JNS153014.

3. Wilson, T.G., Robinson, T., MacFarlane, C., Spencer, T., Herbert, C., Wade, L., Reed, H., and Braybrooke, J.P. (2020). Treating Brain Metastases from Breast Cancer: Outcomes after Stereotactic Radiosurgery. Clin. Oncol. *32*, 390–396. https://doi.org/10.1016/j.clon.2020.02.007.

4. Cortes, J., Rugo, H.S., Cescon, D.W., Im, S.A., Yusof, M.M., Gallardo, C., Lipatov, O., Barrios, C.H., Perez-Garcia, J., Iwata, H., et al. (2022). Pembrolizumab plus Chemotherapy in Advanced Triple-Negative Breast Cancer. N. Engl. J. Med. *387*, 217–226. https://doi.org/10.1056/NEJMoa2202809.

5. Bhandari, S., Dunlap, N., and Kloecker, G. (2021). Radiotherapy in brain metastases from EGFR-mutated non-small cell lung cancer. J. Thorac. Dis. *13*, 3230–3234. https://doi.org/10.21037/jtd-2019-rbmlc-04.

6. Ippolito, E., Silipigni, S., Matteucci, P., Greco, C., Carrafiello, S., Palumbo, V., Tacconi, C., Talocco, C., Fiore, M., D'Angelillo, R.M., and Ramella, S. (2022). Radiotherapy for HER 2 Positive Brain Metastases: Urgent Need for a Paradigm Shift. Cancers *14*, 1514. https://doi.org/10.3390/cancers14061514.

7. de Visser, K.E., and Joyce, J.A. (2023). The evolving tumor microenvironment: From cancer initiation to metastatic outgrowth. Cancer Cell *41*, 374–403. https://doi.org/10.1016/j.ccell.2023.02.016.

8. Pyonteck, S.M., Akkari, L., Schuhmacher, A.J., Bowman, R.L., Sevenich, L., Quail, D.F., Olson, O.C., Quick, M.L., Huse, J.T., Teijeiro, V., et al. (2013). CSF-1R inhibition alters macrophage polarization and blocks glioma progression. Nat. Med. *19*, 1264–1272. https://doi.org/10.1038/nm.3337.

9. Klemm, F., Möckl, A., Salamero-Boix, A., Alekseeva, T., Schäffer, A., Schulz, M., Niesel, K., Maas, R.R., Groth, M., Elie, B.T., et al. (2021). Compensatory CSF2-driven macrophage activation promotes adaptive resistance to CSF1R inhibition in breast-to-brain metastasis. Nat. Cancer *2*, 1086–1101. https://doi.org/10.1038/s43018-021-00254-0.

10. Taggart, D., Andreou, T., Scott, K.J., Williams, J., Rippaus, N., Brownlie, R.J., Ilett, E.J., Salmond, R.J., Melcher, A., and Lorger, M. (2018). Anti-PD-1/anti-CTLA-4 efficacy in melanoma brain metastases depends on extracranial disease and augmentation of CD8(+) T cell trafficking. Proc. Natl. Acad. Sci. USA *115*, E1540–E1549. https://doi.org/10.1073/pnas.1714089115.

11. Friebel, E., Kapolou, K., Unger, S., Núñez, N.G., Utz, S., Rushing, E.J., Regli, L., Weller, M., Greter, M., Tugues, S., et al. (2020). Single-Cell Mapping of Human Brain Cancer Reveals Tumor-Specific Instruction of Tissue-Invading Leukocytes. Cell *181*, 1626–1642.e20. https://doi.org/10.1016/j.cell.2020.04.055.

12. Klemm, F., Maas, R.R., Bowman, R.L., Kornete, M., Soukup, K., Nassiri, S., Brouland, J.P., Iacobuzio-Donahue, C.A., Brennan, C., Tabar, V., et al. (2020). Interrogation of the Microenvironmental Landscape in Brain Tumors Reveals Disease-Specific Alterations of Immune Cells. Cell *181*, 1643–1660.e17. https://doi.org/10.1016/j.cell.2020.05.007.

13. Sudmeier, L.J., Hoang, K.B., Nduom, E.K., Wieland, A., Neill, S.G., Schniederjan, M.J., Ramalingam, S.S., Olson, J.J., Ahmed, R., and Hudson, W.H. (2022). Distinct phenotypic states and spatial distribution of CD8(+) T cell clonotypes in human brain metastases. Cell Rep. Med. *3*, 100620. https://doi.org/10.1016/j.xcrm.2022.100620.

14. Wischnewski, V., Maas, R.R., Aruffo, P.G., Soukup, K., Galletti, G., Kornete, M., Galland, S., Fournier, N., Lilja, J., Wirapati, P., et al. (2023). Phenotypic diversity of T cells in human primary and metastatic brain tumors revealed by multiomic interrogation. Nat. Cancer *4*, 908–924. https://doi.org/10.1038/s43018-023-00566-3.

15. Guldner, I.H., Wang, Q., Yang, L., Golomb, S.M., Zhao, Z., Lopez, J.A., Brunory, A., Howe, E.N., Zhang, Y., Palakurthi, B., et al. (2020). CNS-Native Myeloid Cells Drive Immune Suppression in the Brain Metastatic Niche through Cxcl10. Cell *183*, 1234–1248.e25. https://doi.org/10.1016/j.cell.2020.09.064.

16. Ma, W., Oliveira-Nunes, M.C., Xu, K., Kossenkov, A., Reiner, B.C., Crist, R.C., Hayden, J., and Chen, Q. (2023). Type I interferon response in astrocytes promotes brain metastasis by enhancing monocytic myeloid cell recruitment. Nat. Commun. *14*, 2632. https://doi.org/10.1038/s41467-023-38252-8.

17. Niesel, K., Schulz, M., Anthes, J., Alekseeva, T., Macas, J., Salamero-Boix, A., Möckl, A., Oberwahrenbrock, T., Lolies, M., Stein, S., et al. (2021). The immune suppressive microenvironment affects efficacy of radio-immunotherapy in brain metastasis. EMBO Mol. Med. *13*, e13412. https://doi.org/10.15252/emmm.202013412.

18. Priego, N., Zhu, L., Monteiro, C., Mulders, M., Wasilewski, D., Bindeman, W., Doglio, L., Martínez, L., Martínez-Saez, E., Ramón Y Cajal, S., et al.

(2018). STAT3 labels a subpopulation of reactive astrocytes required for brain metastasis. Nat. Med. *24*, 1024–1035. https://doi.org/10.1038/s41591-018-0044-4.

19. Quail, D.F., and Joyce, J.A. (2017). The Microenvironmental Landscape of Brain Tumors. Cancer Cell *31*, 326–341. https://doi.org/10.1016/j.ccell.2017.02.009.

20. Croci, D., Santalla Méndez, R., Temme, S., Soukup, K., Fournier, N., Zomer, A., Colotti, R., Wischnewski, V., Flögel, U., van Heeswijk, R.B., and Joyce, J.A. (2022). Multispectral fluorine-19 MRI enables longitudinal and noninvasive monitoring of tumor-associated macrophages. Sci. Transl. Med. *14*, eabo2952. https://doi.org/10.1126/scitranslmed.abo2952.

21. Molgora, M., and Colonna, M. (2021). Turning enemies into allies-reprogramming tumor-associated macrophages for cancer therapy. Med *2*, 666–681. https://doi.org/10.1016/j.medj.2021.05.001.

22. Pittet, M.J., Michielin, O., and Migliorini, D. (2022). Clinical relevance of tumour-associated macrophages. Nat. Rev. Clin. Oncol. *19*, 402–421. https://doi.org/10.1038/s41571-022-00620-6.

23. Hedrick, C.C., and Malanchi, I. (2022). Neutrophils in cancer: heterogeneous and multifaceted. Nat. Rev. Immunol. *22*, 173–187. https://doi.org/10.1038/s41577-021-00571-6.

24. Maas, R.R., Soukup, K., Fournier, N., Massara, M., Galland, S., Kornete, M., Wischnewski, V., Lourenco, J., Croci, D., Álvarez-Prado, Á.F., et al. (2023). The local microenvironment drives activation of neutrophils in human brain tumors. Cell *186*, 4546–4566.e27. https://doi.org/10.1016/j.cell.2023.08.043.

25. Veglia, F., Sanseviero, E., and Gabrilovich, D.I. (2021). Myeloid-derived suppressor cells in the era of increasing myeloid cell diversity. Nat. Rev. Immunol. *21*, 485–498. https://doi.org/10.1038/s41577-020-00490-y.

26. Milano, M.T., Grimm, J., Niemierko, A., Soltys, S.G., Moiseenko, V., Redmond, K.J., Yorke, E., Sahgal, A., Xue, J., Mahadevan, A., et al. (2021). Single- and Multifraction Stereotactic Radiosurgery Dose/Volume Tolerances of the Brain. Int. J. Radiat. Oncol. Biol. Phys. *110*, 68–86. https://doi.org/10.1016/j.ijrobp.2020.08.013.

27. Dewan, M.Z., Galloway, A.E., Kawashima, N., Dewyngaert, J.K., Babb, J.S., Formenti, S.C., and Demaria, S. (2009). Fractionated but not single-dose radiotherapy induces an immune-mediated abscopal effect when combined with anti-CTLA-4 antibody. Clin. Cancer Res. *15*, 5379–5388. https://doi.org/10.1158/1078-0432.CCR-09-0265.

28. Vanpouille-Box, C., Alard, A., Aryankalayil, M.J., Sarfraz, Y., Diamond, J.M., Schneider, R.J., Inghirami, G., Coleman, C.N., Formenti, S.C., and Demaria, S. (2017). DNA exonuclease Trex1 regulates radiotherapy-induced tumour immunogenicity. Nat. Commun. *8*, 15618. https://doi.org/10.1038/ncomms15618.

29. Monteiro, C., Miarka, L., Perea-García, M., Priego, N., García-Gómez, P., Álvaro-Espinosa, L., de Pablos-Aragoneses, A., Yebra, N., Retana, D., Baena, P., et al. (2022). Stratification of radiosensitive brain metastases based on an actionable S100A9/RAGE resistance mechanism. Nat. Med. *28*, 752–765. https://doi.org/10.1038/s41591-022-01749-8.

30. Gaebe, K., Li, A.Y., Park, A., Parmar, A., Lok, B.H., Sahgal, A., Chan, K.K.W., Erickson, A.W., and Das, S. (2022). Stereotactic radiosurgery versus whole brain radiotherapy in patients with intracranial metastatic disease and small-cell lung cancer: a systematic review and meta-analysis. Lancet Oncol. *23*, 931–939. https://doi.org/10.1016/S1470-2045(22)00271-6.

31. Perlow, H.K., Dibs, K., Liu, K., Jiang, W., Rajappa, P., Blakaj, D.M., Palmer, J., and Raval, R.R. (2020). Whole-Brain Radiation Therapy Versus Stereotactic Radiosurgery for Cerebral Metastases. Neurosurg. Clin. N. Am. *31*, 565–573. https://doi.org/10.1016/j.nec.2020.06.006.

32. Liau, L.M., Ashkan, K., Brem, S., Campian, J.L., Trusheim, J.E., Iwamoto, F.M., Tran, D.D., Ansstas, G., Cobbs, C.S., Heth, J.A., et al. (2023). Association of Autologous Tumor Lysate-Loaded Dendritic Cell Vaccination With Extension of Survival Among Patients With Newly Diagnosed and Recurrent Glioblastoma: A Phase 3 Prospective Externally Controlled

Cohort Trial. JAMA Oncol. *9*, 112–121. https://doi.org/10.1001/jamaoncol. 2022.5370.

33. Song, E., Mao, T., Dong, H., Boisserand, L.S.B., Antila, S., Bosenberg, M., Alitalo, K., Thomas, J.L., and Iwasaki, A. (2020). VEGF-C-driven lymphatic drainage enables immunosurveillance of brain tumours. Nature *577*, 689–694. https://doi.org/10.1038/s41586-019-1912-x.

34. Harris, M.G., Hulseberg, P., Ling, C., Karman, J., Clarkson, B.D., Harding, J.S., Zhang, M., Sandor, A., Christensen, K., Nagy, A., et al. (2014). Immune privilege of the CNS is not the consequence of limited antigen sampling. Sci. Rep. *4*, 4422. https://doi.org/10.1038/srep04422.

35. Gonzalez, H., Mei, W., Robles, I., Hagerling, C., Allen, B.M., Hauge Okholm, T.L., Nanjaraj, A., Verbeek, T., Kalavacherla, S., van Gogh, M., et al. (2022). Cellular architecture of human brain metastases. Cell *185*, 729–745.e20. https://doi.org/10.1016/j.cell.2021.12.043.

36. Himes, B.T., Geiger, P.A., Ayasoufi, K., Bhargav, A.G., Brown, D.A., and Parney, I.F. (2021). Immunosuppression in Glioblastoma: Current Understanding and Therapeutic Implications. Front. Oncol. *11*, 770561. https://doi.org/10.3389/fonc.2021.770561.

37. Kwak, T., Wang, F., Deng, H., Condamine, T., Kumar, V., Perego, M., Kossenkov, A., Montaner, L.J., Xu, X., Xu, W., et al. (2020). Distinct Populations of Immune-Suppressive Macrophages Differentiate from Monocytic Myeloid-Derived Suppressor Cells in Cancer. Cell Rep. *33*, 108571. https://doi.org/10.1016/j.celrep.2020.108571.

38. Wagner, N.B., Weide, B., Gries, M., Reith, M., Tarnanidis, K., Schuermans, V., Kemper, C., Kehrel, C., Funder, A., Lichtenberger, R., et al. (2019). Tumor microenvironment-derived S100A8/A9 is a novel prognostic biomarker for advanced melanoma patients and during immunotherapy with anti-PD-1 antibodies. J. Immunother. Cancer *7*, 343. https://doi.org/10.1186/s40425-019-0828-1.

39. Akkari, L., Bowman, R.L., Tessier, J., Klemm, F., Handgraaf, S.M., de Groot, M., Quail, D.F., Tillard, L., Gadiot, J., Huse, J.T., et al. (2020). Dynamic changes in glioma macrophage populations after radiotherapy reveal CSF-1R inhibition as a strategy to overcome resistance. Sci. Transl. Med. *12*, eaaw7843. https://doi.org/10.1126/scitranslmed.aaw7843.

40. Kowal, J., Kornete, M., and Joyce, J.A. (2019). Re-education of macrophages as a therapeutic strategy in cancer. Immunotherapy *11*, 677–689. https://doi.org/10.2217/imt-2018-0156.

41. Quail, D.F., Bowman, R.L., Akkari, L., Quick, M.L., Schuhmacher, A.J., Huse, J.T., Holland, E.C., Sutton, J.C., and Joyce, J.A. (2016). The tumor microenvironment underlies acquired resistance to CSF-1R inhibition in gliomas. Science *352*, aad3018. https://doi.org/10.1126/science. aad3018.

42. Bonapace, L., Coissieux, M.M., Wyckoff, J., Mertz, K.D., Varga, Z., Junt, T., and Bentires-Alj, M. (2014). Cessation of CCL2 inhibition accelerates breast cancer metastasis by promoting angiogenesis. Nature *515*, 130–133. https://doi.org/10.1038/nature13862.

43. Loberg, R.D., Ying, C., Craig, M., Day, L.L., Sargent, E., Neeley, C., Wojno, K., Snyder, L.A., Yan, L., and Pienta, K.J. (2007). Targeting CCL2 with systemic delivery of neutralizing antibodies induces prostate cancer tumor regression in vivo. Cancer Res. *67*, 9417–9424. https://doi.org/10.1158/0008-5472.CAN-07-1286.

44. Qian, B.Z., Li, J., Zhang, H., Kitamura, T., Zhang, J., Campion, L.R., Kaiser, E.A., Snyder, L.A., and Pollard, J.W. (2011). CCL2 recruits inflammatory monocytes to facilitate breast-tumour metastasis. Nature *475*, 222–225. https://doi.org/10.1038/nature10138.

45. Kaneda, M.M., Messer, K.S., Ralainirina, N., Li, H., Leem, C.J., Gorjestani, S., Woo, G., Nguyen, A.V., Figueiredo, C.C., Foubert, P., et al. (2016). PI3Kgamma is a molecular switch that controls immune suppression. Nature *539*, 437–442. https://doi.org/10.1038/nature19834.

46. Binnewies, M., Pollack, J.L., Rudolph, J., Dash, S., Abushawish, M., Lee, T., Jahchan, N.S., Canaday, P., Lu, E., Norng, M., et al. (2021). Targeting TREM2 on tumor-associated macrophages enhances immunotherapy. Cell Rep. *37*, 109844. https://doi.org/10.1016/j.celrep.2021.109844.

47. Molgora, M., Esaulova, E., Vermi, W., Hou, J., Chen, Y., Luo, J., Brioschi, S., Bugatti, M., Omodei, A.S., Ricci, B., et al. (2020). TREM2 Modulation Remodels the Tumor Myeloid Landscape Enhancing Anti-PD-1 Immunotherapy. Cell *182*, 886–900.e17. https://doi.org/10.1016/j.cell.2020.07.013.

48. Barry, S.T., Gabrilovich, D.I., Sansom, O.J., Campbell, A.D., and Morton, J.P. (2023). Therapeutic targeting of tumour myeloid cells. Nat. Rev. Cancer *23*, 216–237. https://doi.org/10.1038/s41568-022-00546-2.

49. Mitusova, K., Peltek, O.O., Karpov, T.E., Muslimov, A.R., Zyuzin, M.V., and Timin, A.S. (2022). Overcoming the blood-brain barrier for the therapy of malignant brain tumor: current status and prospects of drug delivery approaches. J. Nanobiotechnology *20*, 412. https://doi.org/10.1186/s12951-022-01610-7.

50. Manthey, C.L., Johnson, D.L., Illig, C.R., Tuman, R.W., Zhou, Z., Baker, J.F., Chaikin, M.A., Donatelli, R.R., Franks, C.F., Zeng, L., et al. (2009). JNJ-28312141, a novel orally active colony-stimulating factor-1 receptor/FMS-related receptor tyrosine kinase-3 receptor tyrosine kinase inhibitor with potential utility in solid tumors, bone metastases, and acute myeloid leukemia. Mol. Cancer Ther. *8*, 3151–3161. https://doi.org/10.1158/1535-7163.MCT-09-0255.

51. Olson, O.C., Kim, H., Quail, D.F., Foley, E.A., and Joyce, J.A. (2017). Tumor-Associated Macrophages Suppress the Cytotoxic Activity of Antimitotic Agents. Cell Rep. *19*, 101–113. https://doi.org/10.1016/j.celrep.2017.03.038.

52. Hao, Y., Hao, S., Andersen-Nissen, E., Mauck, W.M., 3rd, Zheng, S., Butler, A., Lee, M.J., Wilk, A.J., Darby, C., Zager, M., et al. (2021). Integrated analysis of multimodal single-cell data. Cell *184*, 3573–3587.e29. https://doi.org/10.1016/j.cell.2021.04.048.

53. Hafemeister, C., and Satija, R. (2019). Normalization and variance stabilization of single-cell RNA-seq data using regularized negative binomial regression. Genome Biol. *20*, 296. https://doi.org/10.1186/s13059-019-1874-1.

STAR★METHODS

KEY RESOURCES TABLE

REAGENT or RESOURCE	SOURCE	IDENTIFIER
Antibodies		
IF: anti-mouse CD3-AlexaFluor-750 (rat monoclonal 17A2)	RD Systems	Cat#FAB4841, RRID:N/A
IF: anti-mouse CD4-AlexaFluor-488 (rat monoclonal RM4-5)	BioLegend	Cat# 100532, RRID: AB_493373
IF: anti-mouse CD8-AlexaFluor-647 (rat monoclonal 53–6.7)	BioLegend	Cat#100724, RRID:AB_389326
IF: anti-mouse CD45-PE (rat monoclonal 30-F11)	BioLegend	Cat# 103106, RRID:AB_312971
IF: anti-mouse CD31 (goat polyclonal)	RD Systems	Cat#AF3628, RRID:AB_2161028
IF: anti-mouse Ly6B (rat polyclonal)	BioRad	Cat#MCA771G, RRID:N/A
IF: AlexaFluor555 anti-goat IgG (donkey polyclonal)	Invitrogen	Cat# A21432, RRID: AB_2535853
IF: DyLight755 anti-rat IgG (donkey polyclonal)	Invitrogen	Cat#SA5-10031, RRID: AB_2556611
FCM: anti-mouse CD11b BUV661 (rat monoclonal M1/70)	BD Biosciences	Cat#612977, RRID:AB_2870249
FCM: anti-mouse CD11b BV785 (rat monoclonal M1/70)	BioLegend	Cat#101243, RRID: AB_2561373
FCM: anti-mouse CD326 (Ep-CAM) BV421 (rat monoclonal G8.8)	BioLegend	Cat#118225, RRID:AB_2563983
FCM: anti-mouse Ly6G BV605 (rat monoclonal 1A8)	BioLegend	Cat#127639, RRID: AB_2565880
FCM: anti-mouse Ly6C BV711 (rat monoclonal HK1.4)	BioLegend	Cat#128037, RRID: AB_2562630
FCM: anti- mouse Ly6C PE-Dazzle 594 (rat monoclonal HK1.4)	BioLegend	Cat#128043, RRID: AB_2566576
FCM: anti-mouse CD11c BV650 (rat monoclonal N418)	BioLegend	Cat# 117334, RRID: AB_2562415
FCM: anti-mouse PD-L1 PE-Cy7 (rat monoclonal 10F.9G2)	BioLegend	Cat# 124313, RRID: AB_10639934
FCM: anti-mouse CD45 AlexaFluor700 (rat monoclonal 30-F11)	Biolegend	Cat# 103128, RRID: AB_493715
FCM: anti-mouse CD19 PerCP-Cy5.5 (rat monoclonal 6D5)	Biolegend	Cat# 115534, RRID: AB_2072925
FCM: anti-mouse H-2 (MHC-I) PE (rat monoclonal M1/42)	Biolegend	Cat#125505, RRID: AB_1227706
FCM: anti-mouse CD4 PE/Cy5 (rat monoclonal GK1.5)	Biolegend	Cat# 100409, RRID: AB_312694
FCM: anti-mouse CD8b AlexaFluor647(APC) (rat monoclonal YTS256.7.7)	Biolegend	Cat#126612, RRID: AB_2075777
FCM: anti-mouse NK1.1 BV421 (mouse monoclonal PK136)	Biolegend	Cat#108731, RRID: AB_10895916
FCM: anti- mouse NK1.1 BV711 (mouse monoclonal PK136)	Biolegend	Cat# 108745, RRID: AB_2563286
FCM: anti-mouse I-A/I-E (MHCII) BV510 (rat monolonal M5/114.15.2)	Biolegend	Cat#107635, RRID: AB_2561397
FCM: anti-mouse TCRb AlexaFluor488 (Armenian hamster monoclonal H57-597)	Biolegend	Cat#109216, RRID: AB_493345
FCM: anti-mouse CD103 BUV 395 (rat monoclonal M290)	BD Biosceinces	Cat#740238, RRID: AB_2739985
FCM: Zombie NIR™Fixable Viability Dye	BioLegend	Cat#423105
FCM: Purified Rat Anti-Mouse CD16/CD32 (Mouse Fc Block™) (rat monoclonal 2.4G2)	BD Biosceinces	Cat# 553142, RRID:AB_394657
InVivoMAb anti-mouse PD1 (CD279) (rat monoclonal RMP1-14)	Bio X Cell	Cat# BE0146, RRID: AB_10949053
InVivoMAb rat IgG2a isotype control, anti-trinitrophenol (clone 2A3)	Bio X Cell	Cat# BE0089, RRID: AB_1107769
InVivoMAb anti-mouse CD8a (rat monoclonal 2.43)	Bio X Cell	Cat# BE0061, RRID: AB_1125541
InVivoMAb mouse IgG1e3 isotype control (D265A), (monoclonal T9C6)	InvivoGen	Cat# bgal-mab15-1, RRID:N/A
InVivoMAb mouse anti-PD1 (murinized D265A), (monoclonal RMP1-14)	InvivoGen	Cat# mpd1-mab15-1, RRID: N/A
Chemicals, peptides, and recombinant proteins		
TRIzol™ LS Reagent	Thermo Fisher	Cat#10296028
Tween® 20 for molecular biology	Applied Chemicals	Cat#A4974
Triton X-100	Applied Chemicals	Cat#A4975

(Continued on next page)

Continued

REAGENT or RESOURCE	SOURCE	IDENTIFIER
Paraformaldehyde (PFA) 32% solution, EM grade	Electron Microscopy Sciences	Cat#15714-S
L-Lysine	Sigma-Aldrich	Cat#62840
Fetal Bovine Serum (FBS)	Gibco, ThermoFisher	Cat# A5256801
Bovine Serum Albumin	Jackson ImmunoResearch	Cat#001-000-162
Tissue-Tek® O.C.T. Compound	Sakura Finetek	Cat# 45833
Donkey Serum	Sigma Aldrich	Cat#S30-M
Fluorescence Mounting Medium	Dako	Cat#S302380-2
Pentobarbital	CHUV	N/A
D(+)-Sucrose for molecular biology	PanReac AppliChem	Cat#A2211,1000
DMEM/F-12	Gibco, ThermoFisher	Cat#11320033
Penicillin-Streptomycin (10,000 U/mL)	Gibco, ThermoFisher,	Cat# 15070063
Gadovist (Gadobutrol)	Bayer	N/A
UltraPure™ 0.5M EDTA	Invitrogen, ThermoFisher	Cat#15575020
RBC Lysis Buffer (10X)	BioLegend	Cat#420301
Trypan Blue Solution, 0.4%	Gibco, ThermoFisher	Cat#15250061
Brilliant Stain Buffer	BD Biosciences	Cat#563794
Trypsin-EDTA (0.05%), phenol red	Gibco, ThermoFisher	Cat#25300062
Attane™ Isoflurane	Attane	N/A
Buprenorphine, Tamgesic 0.3 mg/ml	Eumedica Pharmaceuticals AG	Cat:#N02AE01
Bupivacaine	Carbostesin, Aspen Pharma Schweiz	Cat:#N01BB01
Lidocain Streuli 2%Inj	Streuli Pharma AG	Cat:#N01BB02
70% Ethanol pads	Fisher Healthcare	Cat#502522446
10% Betadine pads	Purdue Products L.P.	N/A
HBSS, calcium, magnesium, no phenol red	Thermo Fisher Scientific	Cat:#14025092
3M Vetbond	Fisher scientific	Cat:#17150156
Dafalgan	UPSA Switzerland	Cat:#N02BE01
Matrigel	Corning	Cat:#356231
CellTiter-Blue	Promega	Cat:#G8080
DAPI	Thermo Fisher Scientific	Cat:#D1306
Dako mounting medium	Dako	Cat:#S302380
RIPA buffer	Thermo Fisher Scientific	Cat:#89900
Halt Protease inhibitor cocktail	Thermo Fisher Scientific	Cat:#87785
Pierce BCA protein assay kit	Thermo Fisher Scientific	Cat:#23225
RedDot 1 Far-Red Nuclear Stain	Chemie Bruschwig	Cat:#BIO40060-1
CellTrace far red fluorescence	Thermo Fisher Scientific	Cat:#C34572
b-Mercaptoethanol	Thermo Fisher Scientific	Cat:#21985023
HEPES	Thermo Fisher Scientific	Cat:#15630056
mIL2	Milteny	Cat:#130-120-333
CD3/CD28 Dynabeads	Thermo Fisher Scientific	Cat:#11456D
Dimethyl sulfoxide	PanReac AppliChem	Cat:#A3672
Anti-CD11b microbeads	Miltenyi	Cat:# 130-049-601
Critical commercial assays		
Tumor Dissociation Kit, mouse	Miltenyi	Cat#130-096-730
Direct-zol RNA Miniprep kit	Zymo Research	Cat:#R2050
Transcripotor Fisrt Strand cDNA Synthesis Kit	Roche	Cat:#-4379012001
TaqMan Real-Time PCR assays	Thermo Fisher Scientific	N/A
Chromium Single cell 3′GEM kit v3 (10x, 1000077)	10x Genomics	N/A

(Continued on next page)

Continued

REAGENT or RESOURCE	SOURCE	IDENTIFIER
Chromium Single cell B chip kit (10x, 1000074)	10x Genomics	N/A
Chromium single cell 3′ library kit v3 (10x, 1000078)	10x Genomics	N/A
Naive CD8 T cell isolation kit (EasySep)	STEMCELL technologies	Cat:#19858
Anti-Ly6G microbeads	Miltenyi	Cat:#130-120-337
CD8 T cell isolation kit (EasySep)	STEMCELL technologies	Cat:#19858
Deposited data		
Single cell RNA-seq data	This paper	https://www.ncbi.nlm.nih.gov/geo/query/acc.cgi?acc=GSE231657
Mouse reference genome mm10 Ensembl 93 v3.1.0 (Jul 24, 2019)	10x Genomics	https://www.10xgenomics.com/support/software/cell-ranger/latest/release-notes/cr-reference-release-notes#3.1.0
Experimental models: Cell lines		
PyMT-BrM3 (breast-BrM)	Croci et al.[20]	N/A
Experimental models: Organisms/strains		
Mouse: C57BL/6J background	Charles River	N/A
Oligonucleotides		
TaqMan Gene Expression Assay **Ubc** Mm01201237_m1	Thermo Fisher Scientific AG	N/A
TaqMan Gene Expression Assay **Ccl2** Mm00441242_m1	Thermo Fisher Scientific AG	N/A
TaqMan Gene Expression Assay **Ccl5** Mm01302427_m1	Thermo Fisher Scientific AG	N/A
TaqMan Gene Expression Assay **Cxcl9** Mm00434946_m1	Thermo Fisher Scientific AG	N/A
TaqMan Gene Expression Assay **Cxcl10** Mm00445235_m1	Thermo Fisher Scientific AG	N/A
TaqMan Gene Expression Assay **Ifnb1** Mm00439552_s1	Thermo Fisher Scientific AG	N/A
TaqMan Gene Expression Assay **Mx1** Mm00487796_m1	Thermo Fisher Scientific AG	N/A
TaqMan Gene Expression Assay **Ifit1** Mm00515153_m1	Thermo Fisher Scientific AG	N/A
TaqMan Gene Expression Assay **Irf7** Mm00516788_m1	Thermo Fisher Scientific AG	N/A
Software and algorithms		
GraphPad Prism (version 9.0.1)	GraphPad software	https://www.graphpad.com/scientific-software/prism/
FlowJo (version 10.7.1 and 10.8.1)	BD Biosciences	https://www.flowjo.com/
Cell ranger (version 4.0)	10x Genomics	https://support.10xgenomics.com/single-cell-gene-expression/software/pipelines/latest/what-is-cell-ranger RRID:SCR_017344
R (version 4.0.3)	The R Foundation	https://cran.r-project.org/
Cell ranger software (version 4.0)	10x Genomics	https://www.10xgenomics.com/support/software/cell-ranger/latest
Seurat (R package, version 4.0)	Hao et al.[52]	https://github.com/satijalab/seurat RRID:SCR_016341
Tidyverse (R package, version 1.3.0)		https://github.com/tidyverse/tidyverse/releases RRID:SCR_019186

(*Continued on next page*)

Continued

REAGENT or RESOURCE	SOURCE	IDENTIFIER
BioRender	Science Suite Inc.	BioRender Online
ZEN	Zeiss	RRID: SCR_013672
Other		
gentleMACS™ Octo Dissociator with Heaters	Miltenyi	Cat#130-096-427
gentleMACS™ C Tubes	Miltenyi	Cat#130-096-334
BD LSR-II	BD Biosciences	RRID: SCR_002159
BD Aria II (SORP)	BD Biosceinces	RRID:SCR_018934
Axio Scan.Z1 slide scanner	Zeiss	RRID:SCR_020927
Tissue-Tek® Cryomold® Standard	Sakura Finetek	Cat#4557
Rectangular cover glasses	Menzel Gläser, VWR	Cat#631-1339
Multifly® needle, 25G x 3/4″, 80 mm	Sarsted	Cat#85.1642.005
LSRFortessa flow cytometer	BD Biosciences	RRID:SCR_018655
X-RAD SmART system	Precision X-ray irradiation	RRID:SCR_021897
Spark Multimode Microplate reader	TECAN	N/A
3 Tesla Small Animal MR Scanner	Bruker BioSpec	N/A
LEGENDplex mouse anti-virus response panel	Biolegend	Cat:#740622
SKC Inc. C-Chip disposable Neubauer hemacytometers	Thermo Fisher Scientific	N/A
Qubit Fluorometric quantification	Thermo Fisher Scientific	Cat:#Q32851
10x Chromium Controller	10x Genomics	RRID:SCR_019326
High sensitivity next-generation-sequencing fragment analysis	Aligent Technologies	Cat:#DNF-474-0500

EXPERIMENTAL MODEL AND STUDY PARTICIPANT DETAILS

Human brain metastasis samples

All procedures in this study involving the use of tissues derived from human participants were in accordance with the ethical standards of the national research committees and the declaration of Helsinki. For detailed information related to the cohort of human participants (e.g., sex, age, and disease subtype), please see Table S2. Informed consent was obtained for all human subjects participating in this study. The processing of tumor tissue at the Biobank of the Brain and Spine Tumor Center (BB_031_BBLBGT) at the Center Hospitalier Universitaire Vaudois (CHUV, Lausanne, Switzerland), was approved by the Commission cantonale d'éthique de la recherche sur l'être humain (CER-VD, protocol PB 2017–00240, F25/99). All tissue specimens were coded before further handling in accordance with patient privacy regulations.

Mice

All studies utilizing mice were approved by the Institutional Animal Care and Use Committees of the University of Lausanne and Canton Vaud, Switzerland. Animals were bred at the University of Lausanne animal facilities. C57BL/6J mice were initially purchased from Charles River.

Cells

All cell lines were cultured in DMEM/F12 (Thermo Fisher Scientific, Cat# 11320033), supplemented with 10% fetal bovine serum (FBS, Thermo Fisher Scientific, Cat# A5256801) and 1% Penicillin-Streptomycin (Thermo Fisher Scientific, Cat# 15070063) under standard conditions. Cells underwent regular mycoplasma testing using the MycoAlert kit (Lonza, Cat# LT07-118) following the manufacturer's instruction manual. The brain-homing cell line variant has been generated in house.

METHOD DETAILS

Generation of experimental tumor models

For the generation of the intracardiac BrM model, PyMT-BrM3 cells were harvested with Trypsin-EDTA 0.05% (Thermo Fisher Scientific, Cat# 25300054), washed and resuspended in HBSS (Invitrogen, Cat# 14175-053). The concentration was adjusted to 1×10^6 cells per mL and the cells were kept on ice until injection. 100 μL of the cell suspension was injected into the left cardiac ventricle of anesthetized (2% isoflurane inhalation) 6-10 week-old female mice. The correct position was verified by the influx of arterial blood into the syringe upon injection.

For the intracranial BrM model, the cell concentration was adjusted to 5×10^7 cells per mL in HBSS and the cells were kept on ice until injection. 6-10 week-old female mice were anesthetized with 2% isoflurane inhalation. Additionally, 100 μL buprenorphine (0.3 mg/mL Temgesic; Indivior Schweiz) was injected subcutaneously. For local anesthesia, 50μL of a mixture of bupivacaine (2.5 mg/kg, Carbostesin; Aspen Pharma Schweiz) and lidocaine (6 mg/kg, Streuli Pharma) was injected subcutaneously at the injection site. The head was cleaned with 70% ethanol pads (Fisher Healthcare) and 10% betadine pads (Purdue Products L.P.) and a longitudinal incision of the skin was made between the occiput and forehead. A micromotor high speed drill was used to make a hole above the right frontal cortex (2 mm frontal, 1.5 mm lateral from bregma). 25,000 cells in 0.5 μL HBSS were injected using a stereotactic device at a depth of 1.5 mm over at least 5 s (sec). Afterward, the injection site was cleaned with 70% ethanol pads and H_2O_2, and the skin was closed with Vetbond tissue adhesive (3M). Mice received paracetamol (Dafalgan, UPSA) in the drinking water (500 mg per 250 mL) for 7 days, and were monitored during the recovery period at least once daily.

For the generation of the extracranial primary breast tumor model, 6-10 week-old female mice were anesthetized using isoflurane inhalation. PyMT-BrM3 cells (7.5×10^5) were resuspended in 50% Matrigel (Corning, Cat.# 356231) and 50% HBSS, and were injected orthotopically in the mammary fat pad.

Tumor growth monitoring

The monitoring of intracranial tumor growth was performed by magnetic resonance imaging (MRI) using a 3 Tesla Small Animal MR Scanner (Bruker BioSpec). A volume coil was used as transmitter and a channel surface coil was used for signal reception. Mice bearing tumors after an intracardiac injection received one dose of 150 μL Gadobutrol (Gadovist, 1 mmol/mL, Bayer) intraperitoneally 10 min (min) before the MRI. For MRI, the mouse was anesthetized with O2+2% isoflurane inhalation and the respiration and body temperature were monitored. The mouse was imaged in a tail-prone position. Imaging was performed with the Paravision 360 v2.0 software (Bruker). First, a low-quality localizer sequence was performed to locate the brain. For the intracardiac model, a T1-FLASH (fast low angle shot magnetic resonance) sequence was performed with a repetition time (TR) of 253.3 ms, echo time (TE) of 6.288 ms, with 6 averages (NA), and 10 image slices with a thickness (ST) of 0.7 mm. The field of view (FOV) was 20 × 20 mm and a pixel size of 156 x 156 μm. The acquisition time per mouse was 194 s. For the intracranial model, a T2-RARE (turbo rapid acquisition relaxation enhancement) sequence was performed with a repetition time (TR) of 3000 ms, echo time (TE) of 75 ms, with 6 averages (NA), and 10 slices with a thickness (ST) of 0.7 mm. The FOV was 20 × 20 mm and the pixel size 156 x 156 μm. The acquisition time per mouse was 180 s. Tumor volume was determined by analyzing the DICOM files using the MIPAV software (National Institutes of Health, USA).

Tumors growing in the MFP were measured using calipers by determining the two longest perpendicular axes in the x/y plane of the lesions and using Equation 1 to calculate the volume.

$$Volume = \frac{xy^2}{2}$$
(Equation 1)

Radiation treatment of mice

Mice were anesthetized by isoflurane (O2 + 2% isoflurane) inhalation and placed in an X-RAD SmART instrument (Precision X-ray) in a prone position. A 10 × 10 mm collimator was used to deliver the dose precisely. The correct position of the irradiation source was verified by performing live computed tomography imaging and moving the mouse bed according to an MR scan visualizing the tumor. For brain RT, the irradiation source was positioned above the brain sparing the eyes, cerebellum, masticatory apparatus, and upper respiratory tract. For the treatment of MFP tumors, the inguinal lymph nodes were spared. The indicated daily RT dose was delivered in two equal beams positioned at 90° and 270° for the brain and at 20° and 340° for the MFP (beam angle varied from mouse to mouse depending on the location to protect the inguinal lymph nodes).

Systemic treatment of mice

All systemic treatments were delivered intraperitoneally twice per week. If not stated differently, a dose of 250 μg per injection was used. In the case of anti-CD8 (and the corresponding rat IgG2b isotype control antibody), the first injection contained a boost dose of 500 μg. All reagents used are listed in Table S3.

In vitro longitudinal cell viability measurement

The CellTiter-Blue Cell Viability Assay (Promega) was used following the manufacturer's instruction manual. Briefly, 10000 cells per well of a 96-well plate were plated and incubated for 5 h. Afterward, cells were irradiated with indicated doses using the X-RAD SmART system (Precision X-ray) without a collimator. At the indicated timepoints after irradiation, 20 μL per well CellTiter-Blue Reagent was added and the plate was shaken for 10 s. After 4 h incubation under standard cell culture conditions, the plate was shaken again for 10 s and the fluorescence was recorded at 560/590nm using a microplate reader (Tecan). Each condition was measured in triplicate.

Isolation of RNA from cultured cells, synthesis of cDNA and real-time PCR (qPCR)

For RNA extraction, cells were washed and lysed with TRIzol (Life Technology). The Direct-zol RNA Miniprep kit (Zymo Research) was used to purify RNA. 1μg of purified RNA was used to synthesize cDNA using the Transcriptor First Strand cDNA Synthesis Kit (Roche).

The TaqMan system (Life Technology) was used to quantify individual genes (see Key Resource table for the probe IDs). Samples were analyzed in triplicate. Expression of each gene was normalized to *Ubc* as a housekeeping gene and relative expression was calculated with Equation 2:

$$2^{-(\Delta\Delta Ct)}$$

$$\Delta\Delta Ct \; = \; \Delta Ct \, (treated) \; - \; \Delta Ct \, (untreated)$$

$$\Delta Ct \; = \; Ct \, (tested \; gene) \; - \; Ct \, (Ubc)$$

Preparation of tissues from mice

Blood was collected from the submandibular vein using a blood lancet. All other tissues were collected from sacrificed animals. For this, mice were terminally anesthetized with pentobarbital (University of Lausanne, Switzerland) and transcardially perfused with 10mL PBS. Afterward, the processing depended on the downstream analysis.

(1) For flow cytometry analysis and scRNA-seq organs were collected and processed directly.
(2) For cytokine analysis, organs were collected and snap frozen.
(3) For immunofluorescence (IF) analysis, mice were additionally perfused with 10mL periodate-lysine-paraformaldehyde (PLP) buffer and the collected organs were incubated overnight in PLP at 4°C. Afterward, PLP was exchanged for 30% sucrose and the tissue was incubated for another 24 h. The fixed tissue was submerged in OCT compound (Tissue-Tek, Sakura Finetek, Cat# 4583) and frozen at −80°C.

Sectioning, staining and imaging of mouse tissues

Tissue blocks were cut for 5 or 10 μm thick sections and two tissue sections were placed on each slide. Sectioning, and hematoxylin and eosin staining was performed by the UNIL mouse pathology facility. Sections were stored for a maximum time of 3 years at −80°C. For IF staining, frozen sections were thawed for 10 min at ambient temperature, washed, and permeabilized with 0.1% Triton X-100 (PanReac AppliChem, Cat# A4975) for 10 min. Afterward, slides were washed and a hydrophobic circle around the tissue was drawn using the PAP pen (Daido Sangyo). Next, the tissue was washed in PBS, and blocked for 1 h at ambient temperature with 10% donkey serum (EMD Millipore, Merck, Cat# S30-M) in PBS. Primary antibodies (see Table S4) were diluted in 50% blocking buffer (in PBS) and 250μL of the mixture was used to stain one tissue section on each slide overnight at 4°C. The other tissue section on the same slide served as secondary antibody-only control. At the end of the primary antibody incubation, sections were washed 3 × 10 min with PBS. The secondary antibody mix was prepared in the same way as the primary, but additionally contained DAPI (Life Technologies, Cat# D1306) at a 1:3000 dilution. The secondary antibody mix was centrifuged for 15 min at 2000 g and 250μL of the mixture was used to stain the tissue for 1 h at ambient temperature. Both staining steps were performed in a humidified chamber. Finally, sections were washed 3 × 10 min with PBS and mounted with coverslips (Menzel-Gläser, Thermo Scientific, Cat# 631–0973) using the Dako mounting medium (Dako, Cat# S302380). Imaging was performed on the Axio Scan.Z1 slide scanner (Zeiss) using the same acquisition settings within the same experiment to enable comparisons between different samples.

Cytokine measurement

Snap-frozen tumors were thawed on ice and all subsequent steps were performed on ice. For brain tumors, the whole lesion was put into 150 μL of RIPA buffer (Thermo Fisher Scientific, Cat# 89900) supplemented with Halt Protease Inhibitor Cocktail (Thermo Fisher Scientific, Cat# 87785). A high shear homogenizer was used to mince the tissue. 100 μL RIPA buffer was used to flush the homogenizer and the resulting 250 μL protein solution were placed on an orbital shaker for 2 h at 4°C. The protein solution was cleared by centrifugation at 12,000 rpm for 20 min at 4°C. The supernatant was collected and protein concentration was determined using the Pierce BCA Protein Assay Kit (Thermo Fisher Scientific, Cat# 23225) following the manufacturer's instruction manual. MFP tumors were handled in the same way with the exception that large tumors were first cut with a scalpel into small pieces and 0.5–1.5 g were used for protein isolation.

Cytokine quantification was performed with the LEGENDplex Mouse Anti-Virus Response Panel (Biolegend, Cat# 740622) following the manufacturer's instruction manual. A total of 13 molecules were analyzed: IFN-γ, CXCL1 (KC), TNF-α, CCL2 (MCP-1), IL-12p70, CCL5 (RANTES), IL-1β, CXCL10 (IP-10), GM-CSF, IL-10, IFN-β, IFN-α, IL-6. Excel was used to calculate the concentration of each molecule in each sample. Lastly, the detected cytokine concentration was normalized to the total protein concentration measured by BCA followed by calculating the fold-change between treated and untreated samples.

Flow cytometry

For flow cytometry analysis, fresh tissue was collected from sacrificed mice and all the subsequent steps were performed on ice, if not stated otherwise. Tumor tissue was placed in serum-free media and chopped into small pieces with scissors. The Tumor Dissociation Kit for mouse (Miltenyi, Cat# 130-096-730) was used to generate a single cell suspension. After the digestions, cells were filtered through a 40 μm mesh filter and washed. Spleen and lymph nodes were dissociated manually by filtering the tissue through a 40 μm mesh filter with modest force followed by one wash step. Remaining blood cells in tumor, spleen and lymph nodes solutions were lysed with the red blood cell lysis buffer (Biolegend, Cat# 420302) for 10 min on ice followed by washing in FACS buffer (PBS with 2 mM EDTA [Life Technologies, Cat# 15575020] and 0.5% BSA [Jackson ImmunoResearch Cat# 001-000-162]). Whole blood required 2 × 10 min of red blood lysis until clearance. Cell concentration was determined by manual counting using SKC Inc. C-Chip Disposable Neubauer Hemacytometers (Fisher Scientific, Cat# 22-600-100). A maximum of $1.5x10^6$ viable cells were used for staining. First, cells were stained with the Zombie NIR Fixable Viability Kit (Biolegend, Cat# 423105) for 20 min at ambient temperature followed by 10 min incubation with Purified Rat Anti-Mouse CD16/CD32 Mouse Fc Block (BD, Cat# 553142). The staining mix was prepared in Brilliant Stain Buffer (BD, Cat# 563794) using the antibodies and concentrations listed in Table S5. Cells were incubated with the staining mix for 30 min at 4°C, washed at least twice with FACS buffer, and acquired on a BD Fortessa or BD LSR-II. Analysis of the generated flow data was performed using FlowJo (version10.7.1 and 10.8.1).

Sorting and encapsulating cells for single cell RNA-sequencing

Harvested tumors were placed on ice and processed as for flow cytometry with the exception of the viability dye. Instead, samples were stained with mouse Fc block and afterward with the antibody sorting panel composed of anti-CD11b-BV785 (1:320, clone M1/70, Biolegend Cat# 101243) and anti-CD45-AF700 (1:200, clone 30-F11, Biolegend Cat# 103128). Dead cells were excluded using DAPI (Thermo Fisher Scientific, Cat# 62247) and viable cells were additionally stained with RedDot1 Far-Red Nuclear Stain (Chemie Brunschwig Cat# BIO40060-1) following the manufacturer's instruction manual. Total immune cells were sorted as $CD45^+$ DAPI-RedDot-1+ cells using an Aria II (SORP) instrument (BD) into 1.5 mL tubes containing 8 μL cold HBSS. Sorted cells were counted and a total of 16,000 total cells were loaded onto the 10x Chromium Controller following the manufacturer's instruction manual. For the generation of Gel Beads in Emulsion (GEM), Chromium Single Cell 3' GEM Kit v3 (10x, 1000077) and the Chromium Single Cell B Chip Kit (10x, 1000074) were used.

Library preparation and data analysis for single-cell RNA sequencing

Gene expression libraries were prepared using the Chromium Single Cell 3' Library Kit v3 (10x 1000078) following the manufacturer's instruction manual. The quantity of constructed libraries was determined with the Qubit Fluorometric Quantification (Thermo Fisher Scientific, Q32851). Library quality was determined using High Sensitivity Next-Generation-Sequencing Fragment Analysis (Agilent Technologies, DNF-474-0500) and the sequencing was performed by Genewiz Services (http://www.genewiz.com/) on an Illumina HiSeq 2500 or Illumina NovaSeq6000 S4 Flow Cell using a 10x sequencing configuration. Targeted sequencing depth was >20,000 reads per cell.

FastQ files of the sequenced libraries were provided by Genewiz and aligned to the mouse reference genome mm10 (Ensembl 93) 3.1.0 (July 24, 2019) using cell ranger software (version 4.0) from 10x Genomics. Downstream analysis was performed using Seurat (RRID:SCR_016341) package version 4.0[52] in R. For visualization, Seurat and tidyverse (RRID:SCR_019186) packages were used. For quality control, only cells with <10% mitochondrial RNA and 250–3000 total features were retained for further analyses. Samples were integrated with the SCTransform function[53] using the day of sample sorting as the batch parameter. Clustering was performed with 70 dimensions in FindNeighbors and RunUMAP functions and a resolution of 0.45 in the FindClusters function. Cluster-specific genes were identified using the FindMarkers function with FC > 0.25 and at least 25% of cells in each cluster expressing the DEG utilizing the Wilcoxon test. Results were validated by Receiver Operating Characteristic (ROC) analysis in Seurat.

T cell-myeloid co-culture

For the T cell-neutrophil co-culture experiments, naive $CD8^+$ T cells were isolated from spleens of tumor-free C57BL/6J mice using the Naive CD8 T cell isolation kit (EasySep Cat# 19858), labeled with CellTrace Far Red Fluorescence (Thermo Fisher Scientific Cat# C34572), and plated at $8*10^4$ cells per well of a 96-well plate in 100ul of T cell medium composed of RPMI (Thermo Fisher Scientific Cat# 21875034), 10% FBS, 1% Pen/Strep, 50 μM b-Mercaptoethanol (Thermo Fisher Scientific Cat# 21985023), 20 mM HEPES (Thermo Fisher Scientific Cat# 15630056), and 50 U/ml mIL2 (Miltenyi Cat# 130-120-333). T cells were activated with CD3/CD28 Dynabeads (Thermo Fisher Scientific Cat# 11456D). After 24h of culture, neutrophils were isolated. First, single cell suspensions from the bone marrow as well as intra- and extracranial tumors were generated as described above for flow cytometry analysis. Ly6G + cells were isolated using anti-Ly6G microbeads (Miltenyi Cat# 130-120-337) followed by magnetic separation. The Ly6g-flow-through was cryopreserved in 90% FBS (FBS) plus 10% Dimethyl sulfoxide (PanReac AppliChem Cat# A3672). $4*10^4$ Ly6G + neutrophils in 100 μl T cell medium were added to T cells and cultured for 72h.

For the T cell-macrophage co-culture, total $CD8^+$ T cells were isolated from spleens of tumor-free C57BL/6J mice using the CD8 T cell isolation kit (EasySep Cat# 19858), labeled with CellTrace Far Red Fluorescence (Thermo Fisher Scientific Cat# C34572), and plated at $8*10^4$ cells per well of a 96-well plate in 100ul of T cell medium. On the day of the experiment (24h after T cell activation), Ly6G-cells were thawed and labeled with anti-CD11b microbeads (Miltenyi Cat# 130-049-601) followed by magnetic separation to

isolate the Ly6G- CD11b+ population. 4*10^4 myeloid cells in 100 μl medium were add to T cells and cultured for 72h. After the co-culture, non-adherent cells were harvested, stained, and acquired on a BD Fortessa or BD LSR-II instrument.

QUANTIFICATION AND STATISTICAL ANALYSIS

Data analysis and visualization were performed using GraphPad Prism version 9.0.1 or in R Studio (R version 4.0.3) using the tidy-verse package version 1.3.0 or Seurat package version 4.0. Statistical testing depended on data distribution (parametric versus non-parametric), equality or non-equality of variance between groups, and the number of groups to compare. When more than two groups were compared, multiple comparison correction was applied. The exact test and value of * significance used for each experiment is indicated in each figure legend. In general, Type II ANOVA test was used to compare tumor growth curves, the log rank test to compare survival probability, and the Kruskal Wallis test with post-hoc analysis using the Benjamini-Hochberg correction to compare more than two groups. For normally-distributed data with more them two groups unpaired multiple t-tests with Benjamini-Hochberg correction were used. For the comparison of two groups, the Mann–Whitney U test was used. Differential expression in single cell RNA-seq data was calculated utilizing the Wilcoxon test. 'n' in this study represents either the number of biological replicates for *in vitro* experiments or number of mice for *in vivo* experiments.